Viscoelastic-viscoplastic model with ductile damage accounting for tension-compression asymmetry and hydrostatic pressure effect for polyamide 66

Soheil Satouri[a], George Chatzigeorgiou[a], Fodil Meraghni[a]*, Gilles Robert[b]

[a] *Arts et Métiers Institute of Technology, CNRS, Université de Lorraine, LEM3, F-57000, Metz, France*

[b] *DOMO Chemicals – Polytechnyl SAS, Usine de Belle Etoile, 69190 Saint-Fons, France*

Abstract

This paper proposes a model for predicting the complex inelastic mechanical response of polyamide 66. Polyamide 66 is a semi-crystalline pressure-sensitive polymer that exhibits asymmetric yielding behavior, in which the yield strength is slightly higher in compression. With this in mind, an I_1-J_2 yield function considering the asymmetric behavior and the hydrostatic pressure effect is presented and integrated into a phenomenological viscoelastic viscoplastic model accounting for ductile damage. The corresponding thermodynamic framework and constitutive laws are discussed. Then, an experimental approach is presented to identify the model parameters through mechanical tests with different loading paths to capture the active mechanisms. The experimental findings obtained from uni-axial and multi-axial (tension-torsion) mechanical tests and the numerical model are used in an optimization algorithm to identify the model parameters. A parametric analysis is performed to study the effect of the asymmetric behavior on the state variables under different loading conditions using the identified parameters. The present model responses are in good agreement with the experimental data, and the combination of the experimental and numerical results demonstrates and states the asymmetric behavior of polyamide at relative humidity (RH) of 50%, which is captured by the suggested model. It's also worth pointing out that the parametric study conducted on a notched plate using finite element simulations showcases the structural computation capabilities of the proposed model.

Keywords: Thermodynamics, Viscoplasticity, Damage, Tension-compression asymmetry,

*Corresponding author

Email address: fodil.meraghni@ensam.eu (Fodil Meraghni[a])

Polyamide 66, Tension-torsion tests.

1. Introduction

Polyamide 66 has a wide range of applications in the industry thanks to its strong properties and ease of production. It is mostly used in the form of glass-reinforced composites in various mechanical parts, specially in the automotive industry, such as clutch pedals, seat frames, door structures, cooling fans, air filter nozzles, etc. (Pivdiablyk et al., 2020; Obeid, 2016). This widespread applications accompanied by different loading and environmental conditions, and prediction of the mechanical behavior requires an appropriate model with good accuracy considering all active mechanisms namely viscoelastisity, viscoplasticity, and ductile damage. In this respect, many models have been presented in the literature (Praud et al., 2017; Hasan and Boyce, 1995; Schapery, 1997; Abu Al-Rub et al., 2015; Wang et al., 2019; Haddad et al., 2022), which consider the symmetric yield behavior for PA66. However, to develop a more accurate framework, the pressure-sensitivity and asymmetric behavior of polyamides should be also taken into account. In this respect, the dominant mechanisms in PA66 and the corresponding models available in the literature are briefly presented in the following.

As mentioned before, PA66 exhibits complex thermo-mechanical response coupling with viscoelasticity, viscoplasticity, and ductile damage, which have been observed in creep-recovery tests at room temperature (Praud et al., 2017; Benaarbia et al., 2019). Such response is generally driven by the thermal histories governing the crystal perfection index of the polyamide (Uchida et al., 2024). Viscoelasticity is often modeled through either integral or differential frameworks (Miled et al., 2011; Krairi and Doghri, 2014), or using the distribution of non-linear relaxations (DNLR) (Magnenet et al., 2009). In the models with integral form, the stress is derived through the integration of strain over the entire time history. Green, Rivlin, and Spencer (Rivlin, 1983), Pipkin and Rogers (Pipkin and Rogers, 1968), etc., have developed integral forms based viscoelastic models. In the second category, linear viscoelasticity is modeled through differential equations. Maxwell, Kelvin-Voigt, Burgers, and their extensions are the basic models included in this group. Application of the differential formulation with several characteristic times, depending on the material behavior, can capture the viscoelastic mechanism in a wide range of loading frequencies. Furthermore, it allows the development of a thermodynamic framework considering a set of internal state variables

to properly capture the viscous behavior and dissipative mechanisms. It should also be noted that the latter models are simpler to implement numerically than the integral formulation.

Viscoplastic mechanism can be modeled using two main approaches in the literature: unified and non-unified (Chaboche and Rousselier, 1983; Contesti and Cailletaud, 1989). Unified theory considers one single rate-dependent variable for plasticity and creep (i.e. viscosity) (Chaboche, 2008; Barrett et al., 2013), and the non-unified theory considers two separate variables, as time-dependent and time-independent (Cailletaud and Sai, 1995; Velay et al., 2006). The non-unified theory is efficient when viscosity is dominant. However, integration of the non-unified theory to the thermodynamic framework and implementation on the numerical model is more complicated compared to unified approach. Besides assigning appropriate internal state variables, a suitable yield function must be also defined to efficiently describe viscoplastic flow.

Tresca, Mohr-Coulomb, von Mises, Drucker-Prager, and their extensions are some of the yield functions used to describe plastic flow in polymers (Tresca, 1864; Mises, 1913; Coulomb, 1776; Drucker and Prager, 1952). The yield functions are formulated through principal stresses or the stress tensor invariants, I_1, J_2, and J_3. The first invariant of the stress tensor, I_1, represents the hydrostatic pressure effect, and second and third invariants of the stress deviatoric part (J_2 and J_3) correspond to pure shear and rotation, respectively. Von Mises function based on J_2 is frequently used as the yield surface for polymers in the literature (Benaarbia et al., 2019; Nachtane et al., 2022; Praud et al., 2017; Chen et al., 2021). However, the classical von Mises yield surface is not sufficiently accurate to model plastic flow in PA66, particularly under multiaxial loading conditions. Indeed, PA66 is a pressure-sensitive material, and the compressive yield strength is slightly higher than the tensile yield strength (Morin et al., 2011; Dufour et al., 2016; Donato and Bianchi, 2012; Olufsen et al., 2019; Manaia et al., 2020). The Drucker-Prager yield function is more compatible with polymers, in which the tension-compression asymmetry and the hydrostatic pressure effect are taken into account. In this respect, some models have been developed based on Drucker-Prager or its extensions to consider more mechanisms (Raghava et al., 1973; Lee and Ghosh, 1996; Ghorbel, 2008).

When dealing with thermoplastic polymers, the viscoplastic mechanism mentioned above leads to ductile damage which is strongly dependent on the environmental conditions. For modeling damage, different approaches can be adopted using local and nonlocal approaches (Satouri et al., 2022), even for thermoplastic reinforced composites (Satouri et al., 2023a). One approach can be

based on the micromechanics framework, considering the damage as coalescence and widening of voids, as suggested by Gurson (Gurson, 1977). Several studies in the literature have modified the classical Gurson model into a semi-phenomenological model (Chu and Needleman, 1980; Tvergaard and Needleman, 1995; Koplik and Needleman, 1988). Another approach can be based on Continuum Damage Mechanics (CDM), with damage derived from the Thermodynamics of Irreversible Processes (TIP) (Raghavan and Ghosh, 2005). In CDM models, the damage is considered as an internal state variable and the corresponding model parameters can be identified by macroscopic mechanical tests.

This work aims to fill the gaps in available models in the literature and to provide a more accurate analysis of PA66 mechanical responses using a numerical framework which is validated by experimental findings. To this end, an I_1-J_2 yield function, considering tension-compression asymmetry and hydrostaic pressure, is integrated into a Viscoelastic Viscoplastic accounted for ductile Damage model (VEVPD). Accordingly, the thermodynamic framework developed in Praud et al. (2017), is modified based on the new yield function. An innovative experimental approach is presented to identify the model parameters and capture the material asymmetry in an isothermal state at RH=50%. For the first time, the asymmetry parameter, as the ratio between compressive and tensile yield strengths, is identified in the VEVPD framework using tension/torsion experimental data generated from diabolo-shaped samples, whose effect can be observed under tension-compression and multi-axial loading conditions. In this regard, a sensitivity analysis is also provided to highlight the asymmetry parameter effect on the material response under different loading conditions, among them tension-torsion loading configurations. The objective of this study is therefore to provide a suitable framework that can be integrated into a multi-scale model to study the composites behavior. The model is developed based on the small deformation theory, taking into account the fact that PA66-based composites do not undergo large deformations.

This paper is structured as follows: in section 2, the nonlinear inelastic mechanisms of thermoplastics and their pressure-sensitive asymmetrical mechanical response are first discussed, and an appropriate I_1-J_2 yield function is presented, based on which the thermodynamical framework is developed and the constitutive laws are derived; In section 3, the experimental protocol to calibrate and validate the model is presented; in section 4, a parametric study is conducted and the effect of the asymmetry parameter on the stress-strain curves and state variables distribution is explored, and also the capability of the proposed model in the structural computations is investigated through

finite element simulations on a notched plate.

2. Theoretical background and thermodynamical framework

2.1. Nonlinear inelastic mechanisms and constitutive model

In the present study, a viscoelastic viscoplastic rheological model accounting for ductile damage (VEVPD) is adopted to describe the dissipative mechanisms involved during the deformation process of PA66. In what follows, the constitutive laws used for all mechanisms are briefly described.

Viscoelasticity is initiated at the onset of the deformation process. Here, the viscoelastic part of the deformation is described via a differential form relationship considering the Kelvin-Voigt (KV) model. A characteristic time is identified for each KV branch, which provides the time range over which the corresponding branch is expected to be activated. Defining more than one KV branch allows to describe viscoelasticity at several characteristic times Praud et al. (2017), enabling to properly capture viscous effects during the deformation process. To this end, each viscoelastic branch is modeled as a combination of a linear spring and a dashpot (Figure 1). The viscoplastic mechanism is modeled by a parallel assembly of a nonlinear spring, a nonlinear dashpot, and a frictional element in the rheological model (Figure 1). In this study, reduction of the material stiffness is expressed through a scalar internal state variable, D, that describes the ductile damage, is driven by viscoplasticity and introduced to the model through the effective stress concept, $\tilde{\boldsymbol{\sigma}}$ Kachanov (1958); Rabotnov (1968); Chaboche (1997):

$$\tilde{\boldsymbol{\sigma}} = \frac{\boldsymbol{\sigma}}{1-D}. \tag{1}$$

The presence of damage in semi-crystalline polyamide 6 has been observed experimentally by Laiarinandrasana et al. (2010) and Detrez et al. (2011). From a modeling standpoint, Krairi and Doghri (2014) have compared constitutive models for polycrystalline polymer HDPE with and without damage. They concluded that the latter provide better representation of the overall response, since it captured stiffness reduction.

Implementing the present rheological model requires defining a proper yield surface, based on which the plastic flow and subsequently the viscoplastic mechanism is expressed. In the following sections, the pressure sensitivity and asymmetry in tension-compression yield strength is discussed, and a proper yield function is introduced.

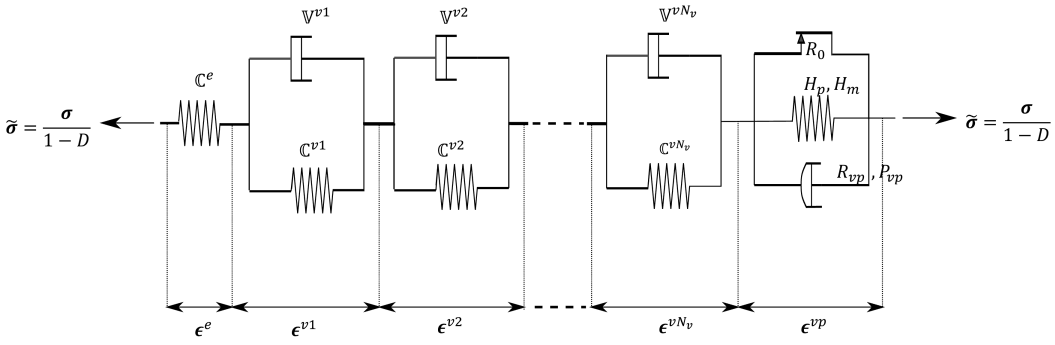

Figure 1: Schematics of the VEVPD rheological model showing N_v viscoelastic branches and a single viscoplastic block subjected to the effective stress.

2.2. I_1-J_2 yield function for asymmetric pressure-dependent material

Thermoplastics are pressure-sensitive materials exhibiting asymmetry in yield behavior(Dufour et al., 2016; Olufsen et al., 2019; Manaia et al., 2020; Ward, 1971; Pae and Bhateja, 1975) The yield strength is expected to be slightly higher in compression than in tension. With this in mind, the von Mises elasticity function based on J_2 (stress invariant) is not sufficiently accurate to describe plastic flow in thermoplastics. In this respect, a number of yield surfaces are proposed in the literature, such as the Mohr-Coloumb and Drucker-Prager models (Raghava et al., 1973; Lee and Ghosh, 1996; Ghorbel, 2008). However, it is often preferred using Drucker-Prager and its extensions to describe the plastic surface in thermoplastics Morin et al. (2011).

Considering an isotropic hardening function, an I_1-J_2 yield surface coupled with damage inspired from Ghorbel (2008), is considered as:

$$f = f^* - R_0 - R, \qquad \text{with} \quad R = H_m r^{H_p}, \tag{2}$$

and:

$$f^* = C_2\sqrt{\tilde{J}_2} + C_1\tilde{I}_1, \qquad C_1 = \frac{m-1}{m(m+1)}, \qquad C_2 = \frac{\sqrt{3}}{m}, \qquad m = \sigma_y^c/\sigma_y^t, \tag{3}$$

where R is the isotropic hardening function, and r is the hardening state variable (also known as accumulated viscoplastic strain). Here, H_m and H_p denote the hardening model parameters. m is the asymmetry parameter introduced to the model as the ratio between compression and tensile elastic limits, and $\tilde{I}_1$ and $\tilde{J}_2$ are respectively first invariant of the effective stress and second invariant

of the effective deviatoric stress tensors, defined as:

$$\tilde{I}_1 = \frac{I_1}{1-D}, \qquad \tilde{J}_2 = \frac{J_2}{(1-D)^2}, \tag{4}$$

with I_1 and J_2 given by:

$$I_1 = \text{trace}(\boldsymbol{\sigma}), \qquad J_2 = \frac{1}{2}\boldsymbol{\sigma}' : \boldsymbol{\sigma}', \tag{5}$$

where $\boldsymbol{\sigma}'$ denotes the deviatoric stress tensor. Figure 2-a shows the yield surface in the 2D field of principal stresses. As observed, an increase in m leads to more pronounced asymmetry in the compression zone. Also, the yield surface is plotted based on the different plastic deformations by giving $m = 1.3$, which is depicted in Figure 2-b. To properly describe the plastic flow in the material, the dissipation positivity must be satisfied. The convexity of the yield function automatically satisfies this condition. The convexity of the proposed yield surface, f, can be easily proved as:

$$\frac{\partial f(\boldsymbol{\sigma}_0)}{\partial \boldsymbol{\sigma}_0} : (\boldsymbol{\sigma} - \boldsymbol{\sigma}_0) \leq f(\boldsymbol{\sigma}) - f(\boldsymbol{\sigma}_0). \tag{6}$$

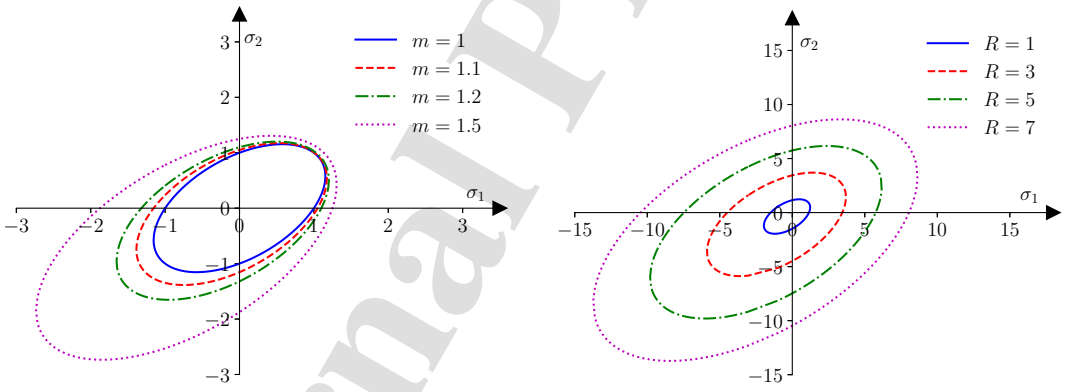

(a) $R = 1$ (b) $m = 1.3$

Figure 2: Impact of the hardening function R and the assymetry coefficient m on the yield surface in the principal stress plane. Parametric study considering a) fixed value of R and varying the value of m, and b) fixed value of m and varying value of R. The value of the hardening function R corresponds to a specific value the hardening state variable r for known parameters H_m and H_p (equation 2). The σ_1 and σ_2 in the graph are nondimensional. For simplicity, R_0 is equal to zero.

The present yield function and the rheological model introduced in the previous sections allow

developing the constitutive laws through a thermodynamical framework, which is given in the next section.

2.3. Constitutive laws

2.3.1. State laws

In the thermodynamical framework, the total strain, $\boldsymbol{\epsilon}$ is the observable state variable, and viscoelastic strains, $\{\boldsymbol{\epsilon}^{vi}\}_{i=1,N_v}$, hardening state variable, r, Damage, D, and viscoplastic strain, $\boldsymbol{\epsilon}^{vp}$, are the internal state variables. Ignoring thermal effects, the Helmholtz free energy function is divided into elastic part, Ψ^e, the set of viscoelastic potentials, $\{\Psi^{vi}\}_{i=1,N_v}$, and the viscoplastic free energy, Ψ^{vp} Praud et al. (2017):

$$\Psi(\boldsymbol{\epsilon},\boldsymbol{\epsilon}^{vi},\boldsymbol{\epsilon}^{vp},r,D)=\Psi^e(\boldsymbol{\epsilon},\boldsymbol{\epsilon}^{vi},\boldsymbol{\epsilon}^{vp},D)+\sum_{i=1}^{N_v}\Psi^{vi}(\boldsymbol{\epsilon}^{vi},D)+\Psi^{vp}(r), \tag{7}$$

with

$$\begin{aligned}\Psi^e&=\frac{1}{2}\left(\boldsymbol{\epsilon}-\sum_{i=1}^{N_v}\boldsymbol{\epsilon}^{vi}-\boldsymbol{\epsilon}^{vp}\right):(1-D)\mathbb{C}^e:\left(\boldsymbol{\epsilon}-\sum_{i=1}^{N_v}\boldsymbol{\epsilon}^{vi}-\boldsymbol{\epsilon}^{vp}\right),\\ \Psi^{vi}&=\frac{1}{2}\boldsymbol{\epsilon}^{vi}:(1-D)\mathbb{C}^{vi}:\boldsymbol{\epsilon}^{vi},\qquad \Psi^{vp}=\int_0^r R(\alpha)\mathrm{d}\alpha,\end{aligned} \tag{8}$$

where $\mathbb{C}^e$ and $\mathbb{C}^{vi}$ are the elastic and viscoelastic stiffness tensors, respectively. The conjugate variables are derived by partial derivatives of the thermodynamic potential with respect to $\boldsymbol{\epsilon}$, $\boldsymbol{\epsilon}^{vi}$, $\boldsymbol{\epsilon}^{vp}$, r, and D:

$$\begin{aligned}\boldsymbol{\sigma}&=\frac{\partial\Psi}{\partial\boldsymbol{\epsilon}}=(1-D)\mathbb{C}_e:\left(\boldsymbol{\epsilon}-\sum_{i=1}^{N_v}\boldsymbol{\epsilon}^{vi}-\boldsymbol{\epsilon}^{vp}\right),\\ \boldsymbol{\sigma}^{vi}&=-\frac{\partial\Psi}{\partial\boldsymbol{\epsilon}^{vi}}=\boldsymbol{\sigma}-(1-D)\mathbb{C}^{vi}:\boldsymbol{\epsilon}^{vi},\qquad \boldsymbol{\sigma}=-\frac{\partial\Psi}{\partial\boldsymbol{\epsilon}^{vp}},\\ R(r)&=\frac{\partial\Psi}{\partial r},\qquad Y=-\frac{\partial\Psi}{\partial D}=\frac{\boldsymbol{\epsilon}^e:\boldsymbol{\sigma}}{2(1-D)}+\frac{1}{2}\sum_{i=1}^{N_v}\boldsymbol{\epsilon}^{vi}:\mathbb{C}^{vi}:\boldsymbol{\epsilon}^{vi}.\end{aligned} \tag{9}$$

It is worth mentioning that the integration of the damage in the viscoelastic free energy potentials (equation (8)) is a choice made on this model, following similar approaches from the literature (Krairi and Doghri, 2014).

2.3.2. Evolution laws

Based on the second principle of thermodynamics, in the form of Clausius-Planck inequality, the dissipated energy rate is always positive or equal to zero. It is expressed as the difference between the stress power, P_m, and the rate of change of the stored energy (density), $\dot{\Psi}$:

$$\begin{aligned}\mathcal{D} &= P_m - \dot{\Psi} \geq 0 \\ &= \boldsymbol{\sigma} : \dot{\boldsymbol{\epsilon}} - \left(\frac{\partial \Psi}{\partial \boldsymbol{\epsilon}} : \dot{\boldsymbol{\epsilon}} + \sum_{i=1}^{N_v} \frac{\partial \Psi}{\partial \boldsymbol{\epsilon}^{vi}} : \dot{\boldsymbol{\epsilon}}^{vi} + \frac{\partial \Psi}{\partial \boldsymbol{\epsilon}^{vp}} : \dot{\boldsymbol{\epsilon}}^{vp} + \frac{\partial \Psi}{\partial r} : \dot{r} + \frac{\partial \Psi}{\partial D} : \dot{D} \right) \geq 0.\end{aligned} \tag{10}$$

Taking into account the expression of the conjugate variables, the dissipation term can be expressed as follows:

$$\mathcal{D} = \sum_{i=1}^{N_v} \boldsymbol{\sigma}^{vi} : \dot{\boldsymbol{\epsilon}}^{vi} + \boldsymbol{\sigma} : \dot{\boldsymbol{\epsilon}}^{vp} - R\dot{r} + Y\dot{D} \geq 0, \tag{11}$$

where $\boldsymbol{\sigma}^{vi}$, R and Y denote the conjugate variables (thermodynamic forcres) corresponding to: viscous stress, the viscoplastic hardening and the energy density release respectively. According to Generalized Standard Materials formalism (GSM), satisfying the Clausius-Planck inequality requires defining the rate of internal state variables through dual dissipation potentials and indicative functions Halphen and Nguyen (1975), which are introduced in the following.

A set of sub-potentials, Ω^{vi}, are introduced to derive the elementary viscoelastic strain rates, $\boldsymbol{\epsilon}^{vi}$, with respect to their associated thermodynamic forces, $\boldsymbol{\sigma}^{vi}$, such that:

$$\Omega^{vi}(\boldsymbol{\sigma}^{vi}, D) = \frac{1}{2}\boldsymbol{\sigma}^{vi} : \frac{\mathbb{V}^{vi\,-1}}{1-D} : \boldsymbol{\sigma}^{vi}, \tag{12}$$

where $\mathbb{V}^{vi}$ denotes the viscosity tensor of the i-th viscoelastic Kelvin-Voigt branch. For each KV branch, a characteristic time, τ^{vi}, can be identified, which corresponds to the viscous behavior of the considered branch. A single viscoelastic branch under a sudden stress, $\boldsymbol{\sigma}_0$, at time t_0 responds through the following equation Ottosen and Ristinmaa (2005):

$$\boldsymbol{\epsilon}^{vi}(t) = \boldsymbol{\epsilon}^{vi}_{\infty}\left[1 - \exp\left(-\frac{t-t_0}{\tau^{vi}}\right)\right], \quad \text{with} \quad \boldsymbol{\epsilon}^{vi}_{\infty} = \mathbb{C}^{vi\,-1} : \boldsymbol{\sigma}_0, \tag{13}$$

with

$$\tau^{vi}\mathbb{I} = \mathbb{C}^{vi\,-1} : \mathbb{V}^{vi}, \quad \tau^{vi} = \frac{\eta^{vi}}{E^{vi}}. \tag{14}$$

The relations between the viscoelastic model parameters are expressed. η^{vi} and E^{vi} denote viscosity parameter and viscoelastic modulus of the i-th viscoelastic branch, respectively. It is noted that,

in the current model, all viscoelastic branches are assumed to have the same Poisson's ratio, equal to the elastic one. This hypothesis allows to reduce the number of required material parameters for calibration. The viscoelastic strain rates are obtained through the derivation of Ω^{vi} with respect to the viscoelastic thermodynamic force:

$$\dot{\boldsymbol{\epsilon}}^{vi} = \frac{\partial \Omega^{vi}}{\partial \boldsymbol{\sigma}^{vi}} = \frac{\mathbb{V}^{vi\,-1}}{1-D} : \boldsymbol{\sigma}^{vi}. \tag{15}$$

According to the J_2-viscoplasticity theory Simo and Hughes (2006), the viscoplastic evolution laws coupled with damage are derived using the Maximum Dissipation Principle (MDP) by considering the following indicative function inspired from damage-plasticity law by Lemaitre (1985):

$$F = f(\boldsymbol{\sigma}, D, r) + f_D, \tag{16}$$

with

$$f_D = \frac{S_D}{(\beta_D + 1)(1-D)} \left(\frac{Y}{S_D} \right)^{\beta_D + 1}, \tag{17}$$

where β_D and S_D are damage-related parameters, and f is given in (2). The damage potential, f_D, drives the evolution of damage in the material. The parameters, S_D and β_D, govern the damage accumulation during the loading process in relation to plastic deformation and mechanical responses. This controls the sensitivity of the damage rate to the energy release, Y, and thereby governs the rate and nature of damage accumulation in the material. The proposed model has been used primarily to predict ductile damage in metals, in which the parameter β_D is commonly positive. Damage growth in metals is slow at the early stages and very rapid at the end of loading. However, damage growth follows a different mechanism in thermoplastics, where the damage accumulation is relatively fast at the beginning and exhibits reduced kinetics thereafter towards steady stable evolution. Such behavior can be captured by considering negative β_D (Krairi and Doghri, 2014; Chen et al., 2023). It is worth pointing out that, if β_D is smaller than -1, a negative damage function, f_D can occur. Nevertheless, the dissipation remains always positive or zero. The viscoplastic evolution and damage laws are expressed as follows:

$$\begin{aligned} \dot{r} &= \dot{\lambda}, \qquad \dot{\boldsymbol{\epsilon}}^{vp} = \frac{\partial F}{\partial \boldsymbol{\sigma}} \dot{\lambda} = \boldsymbol{\Lambda}_{vp} \dot{\lambda}, \\ \dot{D} &= \frac{\partial F}{\partial Y} \dot{\lambda} = \left(\frac{Y}{S_D} \right)^{\beta_D} \frac{\dot{\lambda}}{1-D} = \Lambda_D \dot{\lambda}. \end{aligned} \tag{18}$$

The viscoplasticilty and rate dependency in the permanent deformation zone is modeled by express-

ing the hardening state variable rate with respect to the yield function, f:

$$\dot{r} = \langle \frac{f}{R_{vp}} \rangle_{+}^{1/P_{vp}}, \tag{19}$$

where "$\langle . \rangle_{+}$" denotes the Macaulay brackets, and R_{vp} and P_{vp} are respectively the viscoplastic resistance and exponent.

In this paper, in order to maintain the brevity of the manuscript, detailed formulations and numerical implementation methodology are not presented. In this respect, more details can be found in Praud et al. (2017); Satouri et al. (2022).

3. Model calibration and experimental validation

The parameters, depending on the corresponding mechanism, can be classified into elastic, viscoelastic, viscoplastic, damage, and asymmetry parameters (table 1). It is noted that the Poisson's ratio was considered fixed, equal to 0.3. An appropriate experimental approach is used to capture all active mechanisms, and an optimization method is employed to identify the model parameters. Two types of samples are considered: dogbone and specially designed tension-torsion tubes with a diabolo geometry, as shown in Figure 3. Since polyamide mechanical response is significantly affected by the water content, it is important to ensure the samples relative humidity conditions (RH). Samples are conditioned under RH=50% exposure. At this level of relative humidity and at room temperature, the PA66 has a glass transition temperature up to 25°C (Satouri et al., 2023b) and experiences all mechanisms described earlier during mechanical loading conditions. Dogbone specimens are subjected to monotonic tensile (at different displacement rates), creep recovery (at different levels), and loading-unloading to capture viscoelasticity, viscoplasticity, and ductile damage. The diabolo specimens are subjected to a monotonic proportional tension-torsion tests (at different loading rates) to capture the asymmetric response.

3.1. Experimental setup and procedure

3.1.1. Materials and sample preparation

The polyamide 66 used in this study is supplied by DOMO Chemicals under the commercial name A218 BK 34NG. It is provided in the form of injection-molded plates and diabolo-shape samples. Dogbone samples are cut using water jet hyperbar machining from rectangular injection-molded plates. It's worth mentioning that crystallinity, crystal type and orientation can influence

Table 1: VEVPD model parameter set to be identified in the case of four Kelvin-Voigt branches.

Mechanism	Parameters
Elastic	E
Viscoelastic	$\{E^{vi}, \eta^{vi}, \tau^{vi}\}_{i=1,4}$
Viscoplastic	H_m, H_p, R_{vp}, P_{vp}
Damage	S_D, β_D
Asymmetry	m

material properties. However, for polyamides, these factors have minimal impact due to the short molecular chains, which result in low orientation under molding conditions, mainly guaranteeing isotropic properties. The samples used in this research with the corresponding dimensions are illustrated in Figure 3. To ensure the moisture content, the samples are first exposed to a dry environment at a temperature of 80^oC to release residual humidity up to 0.3%. Then the samples are placed in the hygrometric chamber, Memmert HCP246, at the corresponding temperature and relative humidity (Figure 4). Sample exposure to moisture is implemented in two steps: first, accelerating the process at higher relative humidity and temperature, and then adjusting the considered RH and temperature to homogenize and stabilize the humidity in the sample. Measurement of the mass of reference sample during the conditioning allows determining the water absorption evolution. The sample mass is measured with the accuracy of 0.1 mg. After humidity conditioning, the samples are placed in hermetic envelopes to ensure that the water content remains constant.

3.1.2. Mechanical tests

All mechanical tests have been performed at room temperature. They are designed to: identify the material parameters of the current model and validate the model's ability to describe accurately the material's response. In this respect, the details of the mechanical tests are presented below in two phases: calibration and validation.

In the calibration phase, the mechanical tests must properly capture the dominant mechanisms in the material. Monotonic tests at different displacement rates (0.01 mms^{-1},0.1 mms^{-1},1 mms^{-1}) are performed to capture the time-dependent responses. Loading-unloading test is implemented at 0.1 mms^{-1} displacement rate to capture the damage evolution in the material. Viscoelastic and

a) dogbone sample

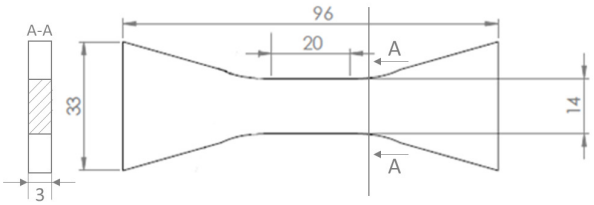

b) Dimensions of dogbone sample

c) Diabolo sample

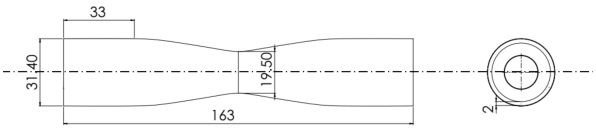

d) Dimensions of diabolo sample

Figure 3: Dogbone and diabolo samples geometries and the corresponding dimensions.

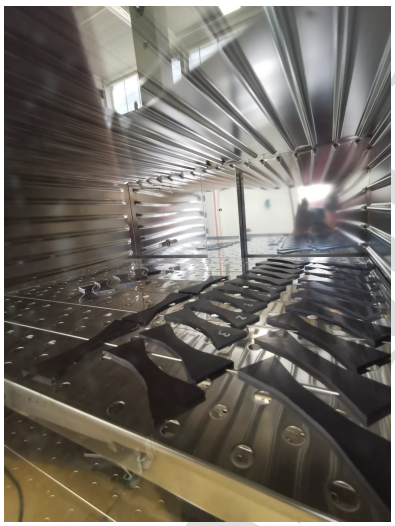

a) dogbone samples

b) Diabolo samples

Figure 4: Dogbone and diabolo samples under exposure of RH=50% conditioning in the hygrometric chamber. The samples are first dried, then exposed to 50% relative humidity until their weight is stabilized.

viscoplastic mechanisms are captured by creep-recovery tests at 50% and 70% of the ultimate force, F_{ult}. The sample is subjected to the constant force for 5 min, then allowed to recover for another 5 min. All of these tests are performed on dogbone samples. To capture the asymmetric yield behavior, the specimens must be subjected to multi-axial tension-compression loading. However, it is too complex to impose compression on PA66 without any buckling. To address this, specially designed diabolo samples (Zine et al., 2011; Goutal, 2020; Głowacka et al., 2022) are proposed and to avoid the likely buckling effect in the responses, the diabolo samples are subjected to proportional tension-torsion loading instead. Loading in two directions are imposed simultaneously with the rates of $0.5\,\text{mm}\,\text{s}^{-1}$ in tension and $0.3^{\text{o}}\,\text{s}^{-1}$ in torsion. More details about mechanical tests are shown schematically in Figure 5.

For the validation phase, a cyclic tensile test is performed at 0.1 mms^{-1}. The loading-unloading test is also considered at a different displacement rate (0.05 mms^{-1}). The stepped creep-recovery test for validation phase is conducted with loading at 0.1 mms^{-1} displacement rate and loading levels of 50%, 70% and 90% of the ultimate force, F_{ult}. Moreover tension-torsion multi-axial loading, similar to the calibration phase, is performed in two directions simultaneously with the rates: i) $0.05\,\text{mm}\,\text{s}^{-1}$ and $0.03^{\text{o}}\,\text{s}^{-1}$, and ii) $5\,\text{mm}\,\text{s}^{-1}$ and $3^{\text{o}}\,\text{s}^{-1}$ (Figure 6).

As previously mentioned, the samples are all conditioned to RH=50%. Zwick-Roell Z050, 50kN is employed to perform tensile tests on dogbone samples. To improve the accuracy of the experimental results, a sample setting tool is designed to keep the dogbone sample properly aligned with the machine loading axis (Figure 7). Longitudinal tensile strain is measured using an extensometer with 25 mm gauge. It should be noted that engineering strains and stresses are considered here, and stress is computed based on the initial cross-section of the specimen due to small deformation framework. The multi-axial tension-torsion tests on the diabolo sample are performed through a tension-torsion Zwick-Roell hydraulic machine with 25kN maximum load and 250 Nm as the maximum torque. Special grips are designed to match the diabolo specimens to the machine axes in order to properly introduce the combined load and also maintain the sample cylindrical cross-section (Figure 8).

3.2. Experimental results

In this section, the findings of the mechanical tests mentioned earlier are discussed. The material at RH=50% is expected to exhibit mostly inelastic nonlinear time-dependent behavior and

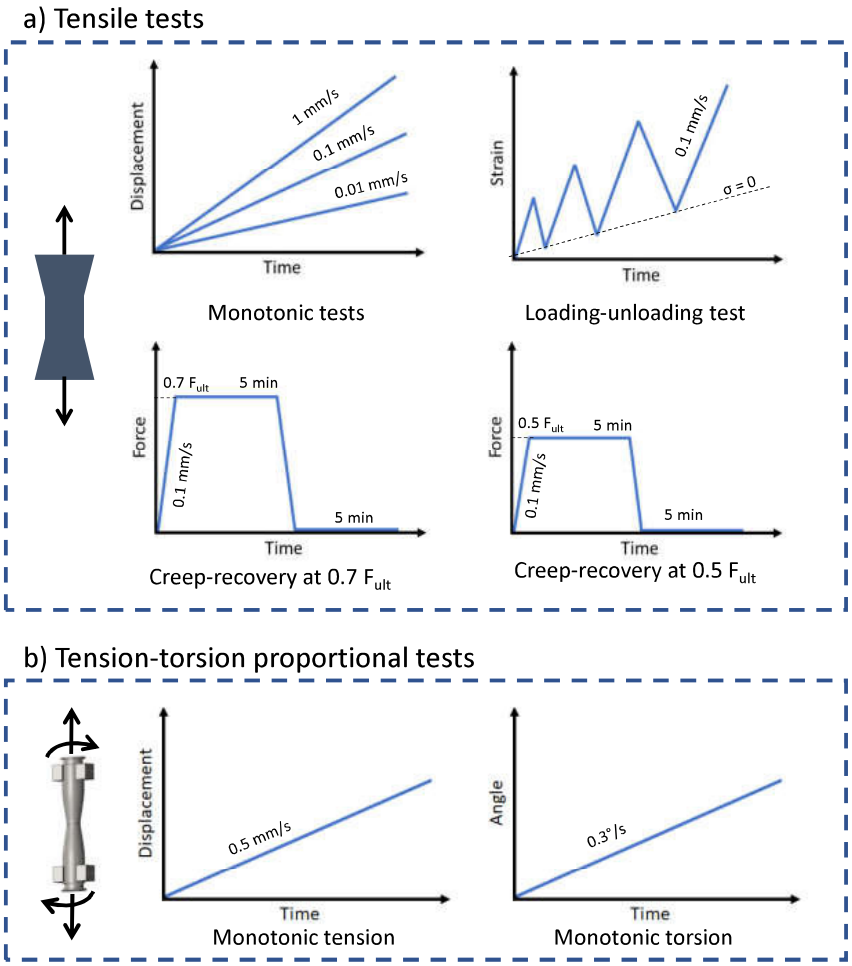

Figure 5: Schematics of mechanical tests utilized for the calibration procedure: a)tensile tests, b) tension-torsion tests (loading in two directions are imposed simultaneously with the given rates).

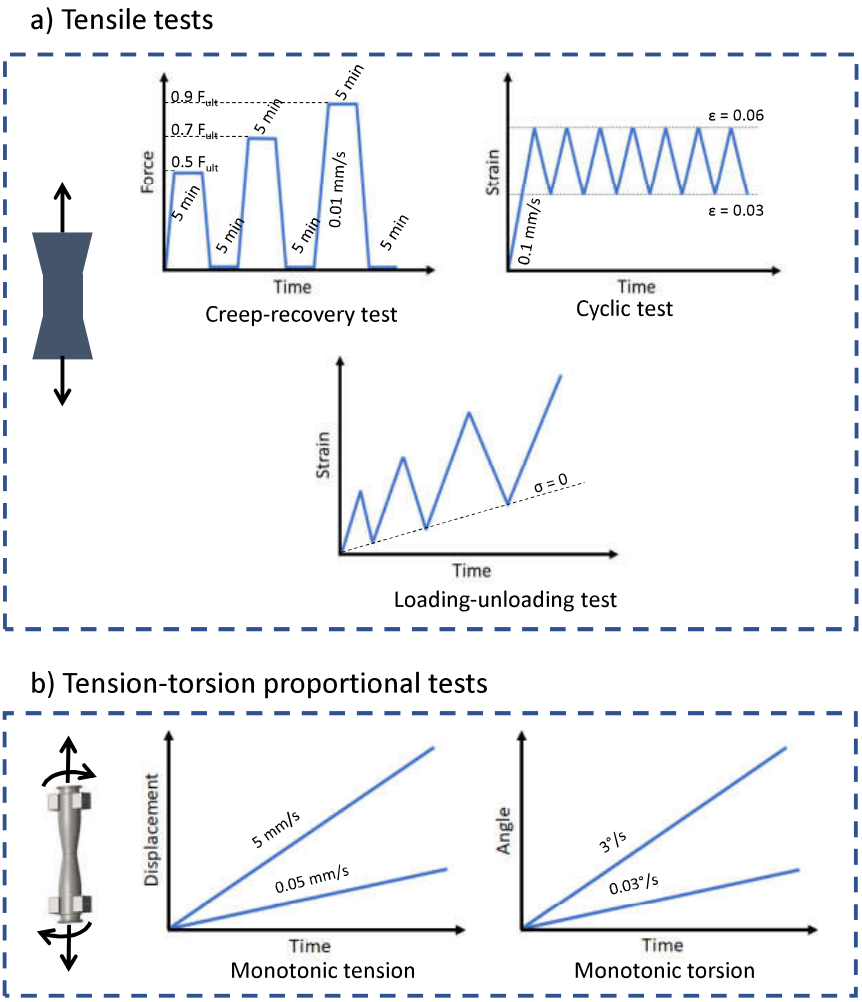

Figure 6: Schematics of mechanical tests employed for the experimental validation of the model: a)tensile tests, b) tension-torsion tests (loading in two directions are imposed simultaneously with the given rates).

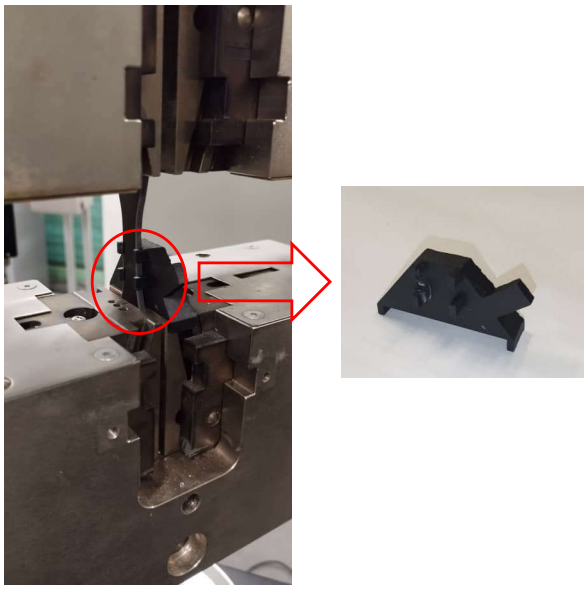

Figure 7: Sample setting tool to keep the dogbone sample aligned with the machine. The tool is removed before testing begins.

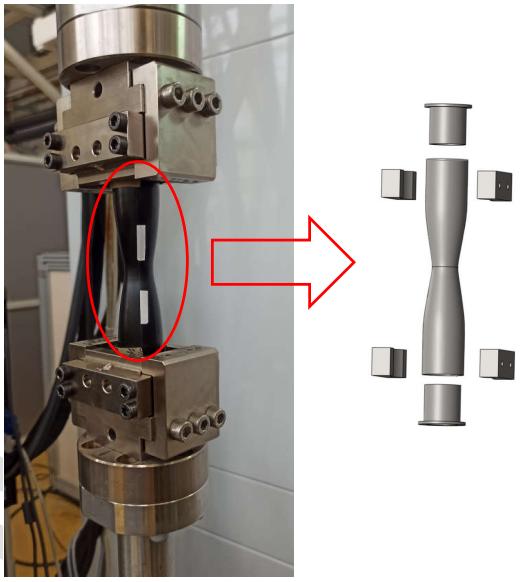

Figure 8: Assembly of grips and diabolo shape sample for tension-torsion tests. The supports are designed to keep the cross-section of the samples circular.

plasticity-induced ductile damage. Figure 9 provides a comparison of the specimen shape before and after loading, in which plastic deformation can be detected using the white stickers on the specimen. The experiments conducted on the diabolo samples provide the overall force-displacement and moment-angle curves shown in Figure 10. As expected, overall force reaches higher values when the sample is subjected to faster loading rate. Figure 11 displays the stress-strain curves obtained from monotonic tests on dogbone samples and at three different displacement rates: 0.01, 0.1 and 1 $mm\,s^{-1}$. As expected, the larger the displacement rate, the higher the stress. The stress-strain curve related to the loading-unloading test is plotted and shown in Figure 12. As observed, after each unloading, the loading slope decreases, demonstrating material damage. The creep-recovery tests at 50% and 70% levels of the ultimate force are performed, and the results are depicted as stress-strain curves in Figure 13. The ultimate force is identified using the monotonic tests.

Figure 9: Plastic elongation and damage induced by tension-torsion loading of the diabolo sample exposed to RH=50%.

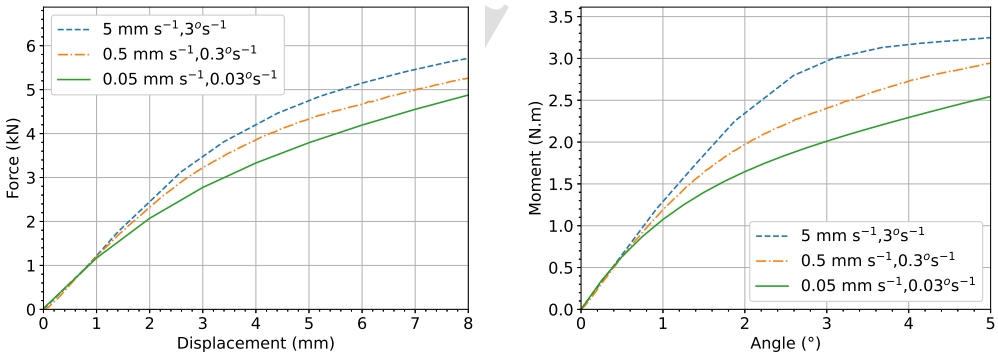

a) Monotonic tension b) Monotonic torsion

Figure 10: Force-displacement and moment-angle curves of the tension-torsion tests on the diabolo sample at different loading rates. It is worth noticing that tension and torsion are imposed simultaneously.

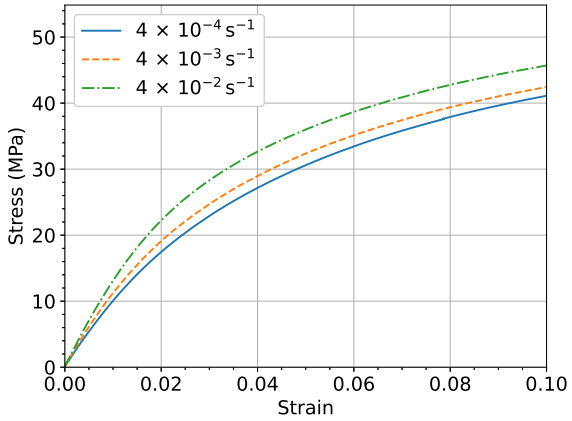

Figure 11: Stress-strain curves of the monotonic tests on the dogbone samples at different strain rates.

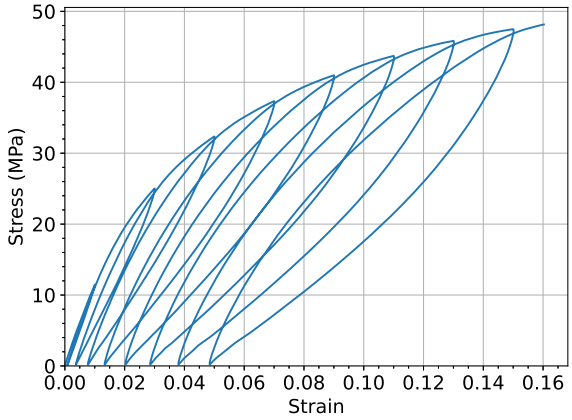

Figure 12: Stress-strain curves of the loading-unloading test on the dogbone sample.

3.3. Model calibration and comparison with experimental results

For the identification of the model parameters, the tests dedicated to the calibration are utilized. To this end a cost function between experimental and numerical results is defined and an optimization approach is employed to minimize it. Here, the numerical results are generated through two different tools. For tensile tests including monotonic, loading-unloading, and creep-recovery on the dogbone samples, a home-made 0D solver is used, in which the results are obtained only for a single

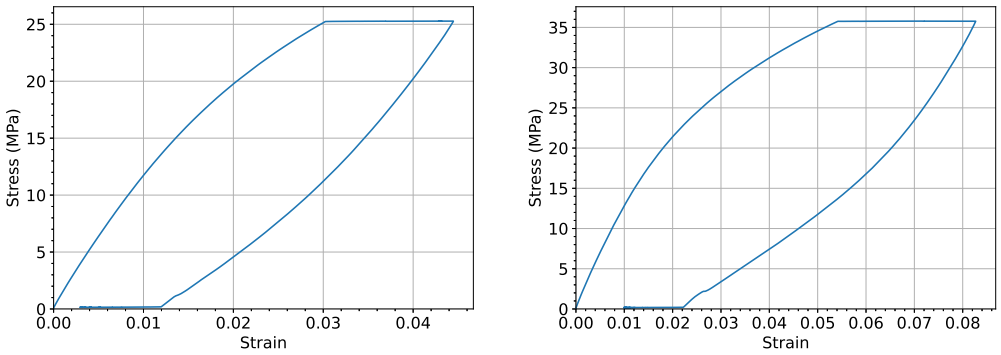

a) Creep-recovery at $0.5\,F_{\text{ult}}$ b) Creep-recovery at $0.7\,F_{\text{ult}}$

Figure 13: Stress-strain curves of the creep-recovery tests on the dogbone samples obtained for two creep loading levels.

point. However, tension-torsion tests on diabolo samples require model implementation in an FE solver and the problem is solved for the whole structure, then the overall force-displacement and moment-angle curves are compared to the experimental results. In the optimization algorithm, at each step, all experimental results are compared with their numerical counterparts. With this in mind, the results produced by the FE solver need to be fast enough to accelerate the optimization procedure. Since the diabolo geometry and the loading conditions are symmetrical, only a 10° slice is considered for each analysis with 84 elements and 340 nodes, as shown in Figure 14b, using 8-node brick finite element type (C3D8). A 10° slice is chosen instead of axisymmetric analysis to avoid modifying the developed 3D User Material (UMAT) for ABAQUS. The analysis has been carried out using the cyclic symmetry boundary conditions of ABAQUS, which are typically adopted to model repeating patterns in structures. The application of the loading and boundary conditions is achieved in four steps:

- Defining Master and Slave Surfaces; The aim is to apply periodicity on the two surfaces of the diabolo-like shape sector.
- Coupling Constraints; This step requires the definition of reference points on the symmetry axis. The region tied to the reference point is applied to the surface as the clamps/grips are installed in the experimental mechanical setup.

- Applying torsion and tension loads at the reference points; The displacement-controlled tensile load is applied along the symmetry axis, and the torsion is applied around this axis (anti clockwise) at the same reference point. Displacement and all rotations are fixed at the second reference point of the sector.

- Considering the Cyclic Symmetry Interaction; The cyclic symmetry feature in ABAQUS is used to specify symmetry along the diabolo axis. Given the symmetry axis and the number of sectors in 360^o, the results are translated for a full diabolo-shape structure.

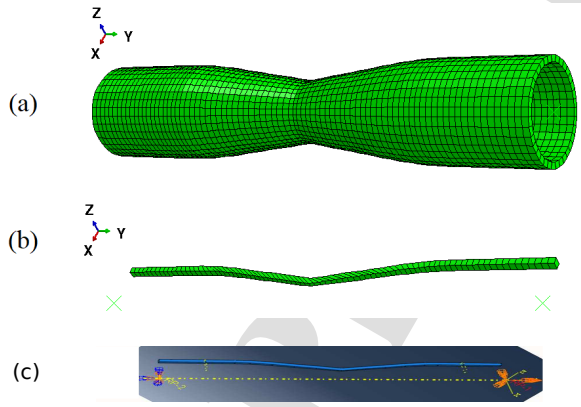

Figure 14: Geometries of finite element models designed in ABAQUS: a) full-structure diabolo model; b) a slice of diabolo model (1/36 or 10^o); c) the discritized sector with the two reference points used for the application of the displacement-controlled torsion and tension boundary conditions.

An optimization algorithm based on the Nelder-Mead approach (Nelder and Mead, 1965) is used to identify the model parameters. To minimize a function containing n variables, a geometrical shape with $n+1$ vertices named "simplex" is defined in an n-dimensional domain as $\mathbb{R}^n$. For example, a triangle for $n = 2$, a tetrahedron for $n = 3$, and so on. At each step, the cost function values at each vertex are calculated, then sorted and reconfigured or replaced by new values according to the defined phases. The process ends when the standard deviation of the function values is sufficiently close to zero. For more details and the formulations of Nelder-Mead approach, the interested reader is referred to Nelder and Mead (1965); Singer and Nelder (2009). In this work, Nelder-Mead algorithm is used through a standard python library. Since, in the optimization process, initial values are of great importance and can affect the convergence or divergence

of the optimization, minimization of the cost function is implemented through a special multi-step strategy that uses experimental data step by step as follows:

- o monotonic loading tests data.
- o monotonic loading, and loading-unloading tests data.
- o monotonic loading, loading-unloading, and creep-recovery loading at 50% of F_{ult} tests data.
- o monotonic loading, loading-unloading, creep-recovery loading at 50% of F_{ult}, and creep-recovery loading at 70% of F_{ult} loading tests data.
- o monotonic loading, loading-unloading, creep-recovery loading at 50% of F_{ult}, creep-recovery loading at 70% of F_{ult} loading, and tension-torsion loading tests data

The list of unknown material parameters are obtained from the minimization problem,

$$p = \underset{p \in S}{\text{ArgMin}}(C(p)), \tag{20}$$

where

$$\begin{aligned} C(p) \quad = \quad & \sum_{i=1}^{N_1} \left[\frac{\sigma_i^{\text{num}}(p) - \sigma_i^{\text{exp}}}{\sigma_i^{\text{exp}}} \right]^2 + \sum_{j=1}^{N_2} \left[\frac{F_j^{\text{num}}(p) - F_j^{\text{exp}}}{F_j^{\text{exp}}} \right]^2 \\ & + \sum_{k=1}^{N_3} \left[\frac{M_k^{\text{num}}(p) - M_k^{\text{exp}}}{M_k^{\text{exp}}} \right]^2 . \end{aligned} \tag{21}$$

In the above expression, σ_i, F_j and M_k denote the stress (N_1 available data), the force (N_2 available data) and the moment (N_3 available data) respectively, while the superscripts num and exp refer to modeling and experimental values respectively.

It should be noted that the parameters identified at each step are used as the initial parameters set for the next step. Using the approach expressed above, the material properties are obtained and the curves are plotted and shown in the Figures 15 to 20. It is worth mentioning that, due to the multiple types of nonlinear mechanisms and the large number of parameters, there is no unique solution in the minimization of the cost function. It is expected that a local minimum has been achieved. This is commonly observed in the literature for the calibration of such complex constitutive laws using inverse methods. In the calibration phase, as observed in Figures 15 and 16, the experimental and numerical responses obtained from monotonic tests (tensile and tension-torsion) have good agreement with each other. Also, loading-unloading experimental data are quite

close to the numerical ones (Figure 17). However, some discrepancies in the creep-recovery tests are observed which can be due to including many mechanisms at the same time (Figure 18). Using the above mechanical tests and the proposed optimization algorithm, dominant mechanisms are captured and the corresponding parameters are identified and listed in Table 2. In this study, the asymmetry parameter, m, is identified for the first time at $RH = 50\%$ and is equal to 1.05. In other words, the compressive yield strength is slightly higher than the tensile yield strength, resulting in asymmetrical behavior under tension-compression and multi-axial loading conditions. It should be noted that the identified m parameter fits well within the range of other types of semi-crystalline polymers (Ghorbel, 2008).

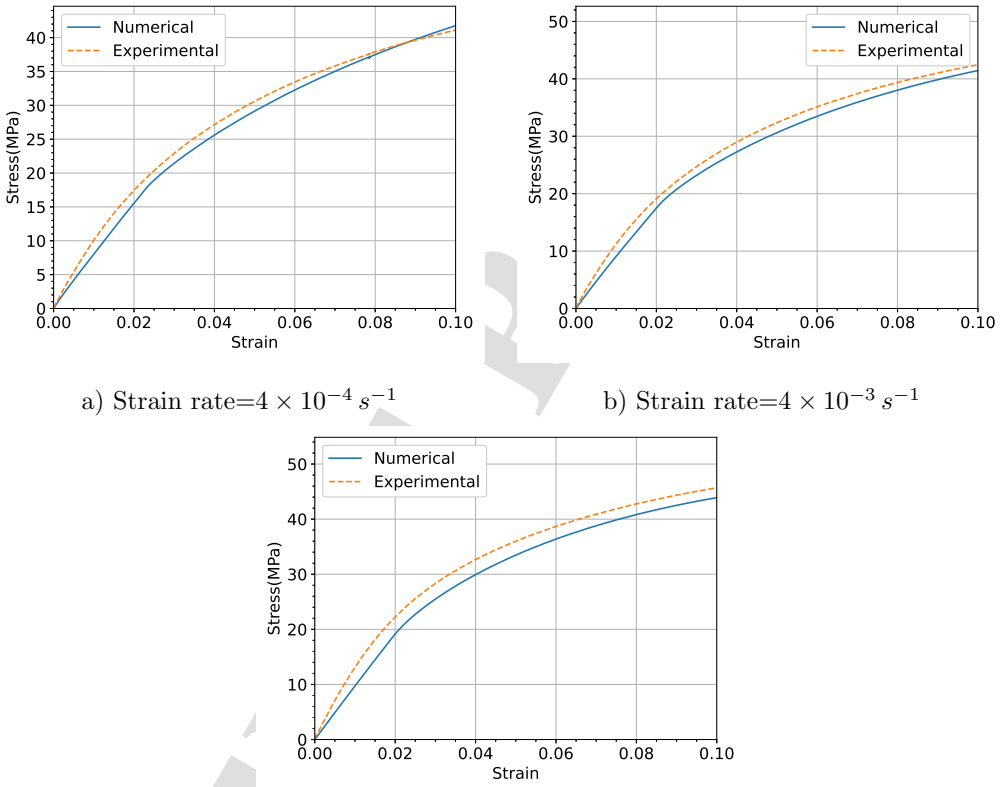

a) Strain rate=$4 \times 10^{-4}\, s^{-1}$

b) Strain rate=$4 \times 10^{-3}\, s^{-1}$

c) Strain rate=$4 \times 10^{-2}\, s^{-1}$

Figure 15: Comparison of the numerical and experimental results for monotonic tests on dogbone samples at different strain rates in the calibration procedure.

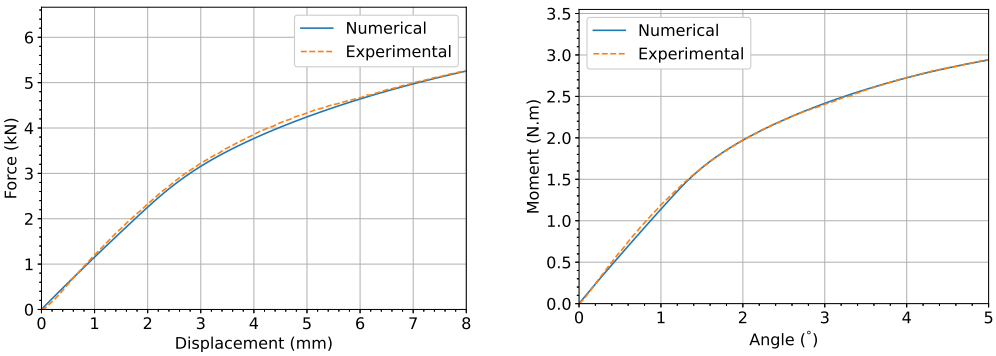

a) Monotonic tension b) Monotonic torsion

Figure 16: Calibration results of the tension-torsion tests on the diabolo at 0.5 mms^{-1} and $0.3^o s^{-1}$.

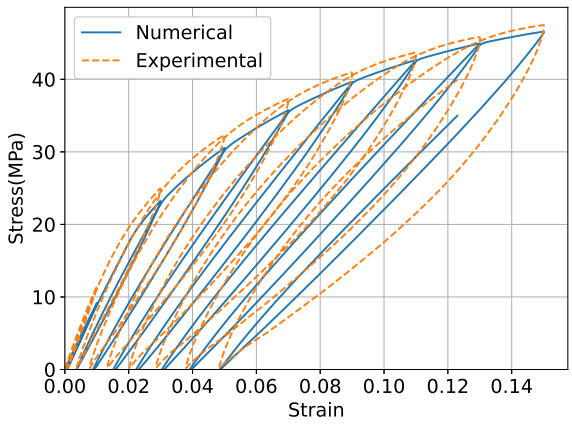

Figure 17: Comparison of the numerical and experimental results for loading-unloading tests on dogbone samples in the calibration phase.

Table 2: Calibrated model parameters at RH=50%.

Mechanism	Parameters (unit)	Identified value
Elastic	E (MPa)	988.95
Viscoelastic	E^{v1} (MPa)	36396.15
	E^{v2} (MPa)	5765.97
	E^{v3} (MPa)	5924.76
	E^{V4} (MPa)	83879.34
	τ^{v1} (s)	0.8
	τ^{v2} (s)	8
	τ^{v3} (s)	80
	τ^{v4} (s)	800
Viscoplastic	H_m (MPa)	996.83
	H_p $(-)$	0.76
	R_{vp}(MPa.s$^{P_{vp}}$)	24.83
	P_{vp} $(-)$	0.37
	R_0 (MPa)	17.04
Damage	S_D (MPa)	26.78
	β_D $(-)$	-0.83
Asymmetry	$m(-)$	1.05

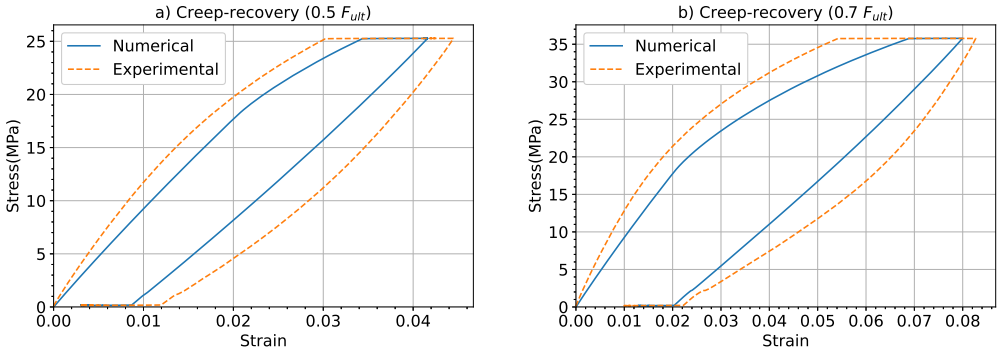

a) Creep-recovery with $0.5\,F_{\text{ult}}$ b) Creep-recovery with $0.7\,F_{\text{ult}}$

Figure 18: Comparison of the numerical and experimental results for creep-recovery tests on dogbone samples at different loading levels in the calibration phase.

At the validation stage, the identified parameters are used to predict material behavior at different loading rates and conditions. Figures 19 to 21 show the comparison between experimental and numerical results in the validation phase. Figures 19 and 20 compare force-displacement curves obtained from monotonic tension-torsion tests on diabolo samples at the rates 10 times higher and 10 times lower than in the calibration phase (0.05 mms^{-1} and $0.03^o s^{-1}$; 5 mms^{-1} and $3^o s^{-1}$). The numerical model provides overall good agreement with experimenal responses. However, there are some discrepancies in the moment-angle curves (Figures 19-b and 20-b), which may be due to structural and geometrical factors that are not captured in the present framework. Figure 21 compares the stress-strain curves of numerical and experimental results from tests on dogbone samples (creep-recovery at different steps, cyclic, and loading-unloading tests). Similarly, there is a good agreement between numerical and experimental responses, but also some differences. In Figure 21-a, the creep at 70% of F_{ult} is estimated below that of experimental values which may be due to the fact that the creep calibration is limited to characteristic times less than 800 s. It should be also noted that the proposed constitutive law does not account for the coupled thermomechanical effects that appear during cyclic loading. Such effects have been partially addressed in an older version of the model without the asymmetry effect by Benaarbia et al. (2019). In addition, the tension-compression assymetry is captured by the model with the use of a single parameter without accounting for J_3 effects. These factors may contribute in the model's accuracy.

Overall, the model's accuracy can be considered satisfactory for industrial applications, given the number of nonlinear mechanisms and the four different types of loading conditions included in this research (monotonic, load-unload, creep and tension-torsion). Of course, the proposed constitutive law is suitable in the range of small strains. It is recalled that the ultimate goal is to integrate the constitutive law in multi-scale frameworks for the study of polymer based composites under small deformation conditions. It should be reported that for unreinforced semi-crystalline polymers, there are suitable models to capture the response under large deformations, as for instance the relevant work by Reuvers et al. (2024) devoted to polyamide 6 blends. The latter article aimed to capture both uniaxial and relaxation response.

So far, a new constitutive model including tension-compression asymmetry and hydrostatic pressure effect has been proposed, and the dominant mechanisms have been captured using mechanical tests, then the proposed framework has been calibrated and validated using experimental data. In the next section, a parametric study is implemented on the present model to investigate asymmetric behavior under tension-compression and multiaxial loading conditions.

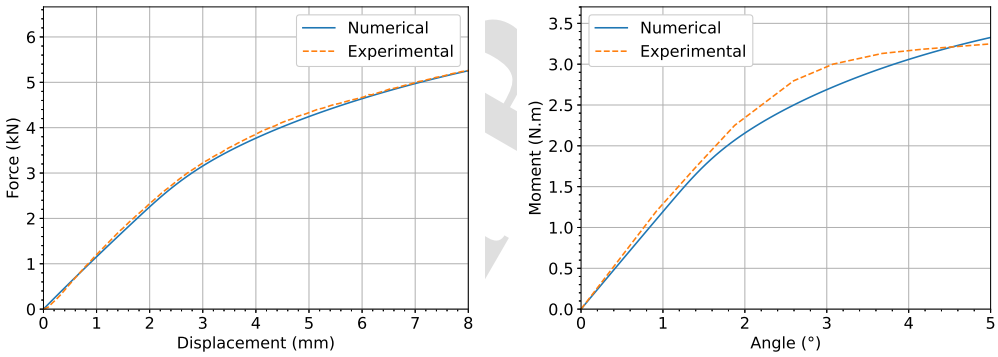

a) Force-displacement b) Moment-angle

Figure 19: Comparison between numerical and experimental results through force-displacement and moment-angle curves of multi-axial tension-torsion test at 5 mms^{-1} and $3^o s^{-1}$ in the experimental validation of the model.

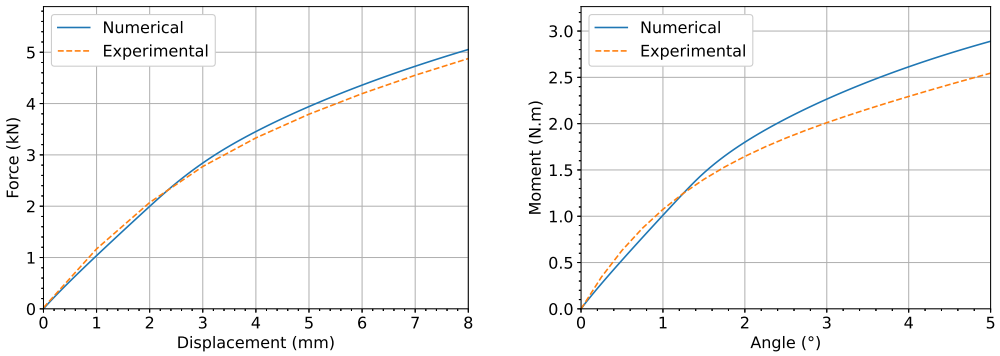

a) Force-displacement b) Moment-angle

Figure 20: Comparison between numerical and experimental results through force-displacement and moment-angle curves of multi-axial tension-torsion test at 0.05 $\mathrm{mm}s^{-1}$ and $0.03^{o}s^{-1}$ in the validation phase.

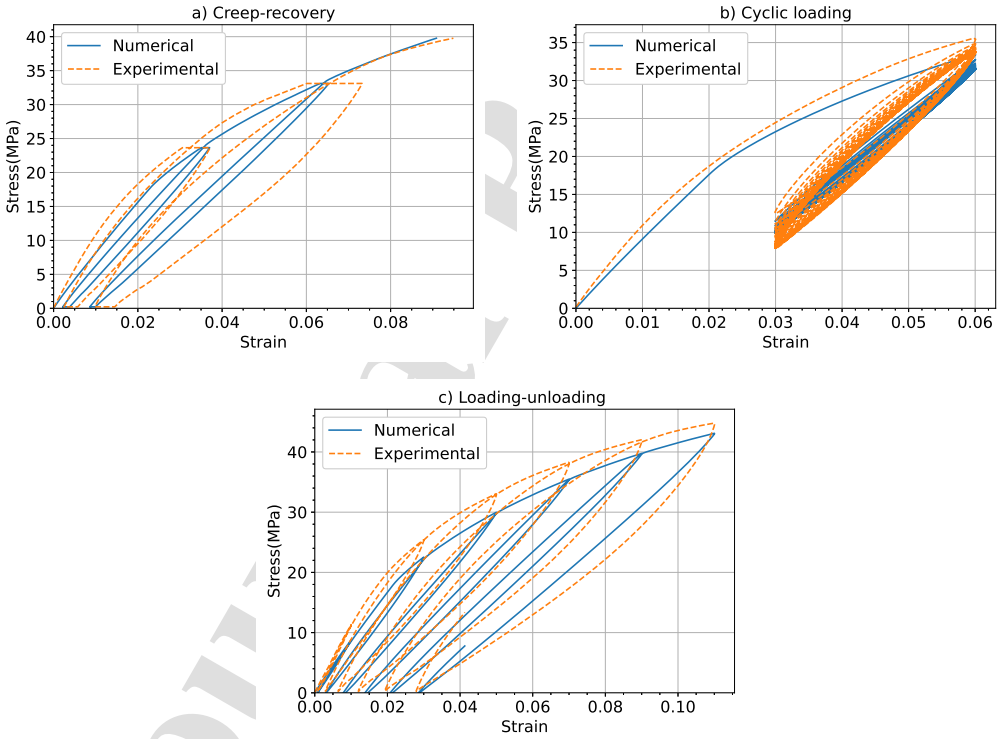

Figure 21: Validation of results through stress-strain curves of creep-recovery, cyclic tests, and loading-unloading.

4. Parametric study

4.1. Mechanical responses investigation using the 0D solver

In this section, the home-made 0D solver, used for the model calibration earlier, is employed to conduct a parametric study. Material properties identified in the previous section (Table 2) are used for the analyses. It should be noted that in the 0D solver, loading conditions are applied to a single point. In all loading conditions, the strain rate is set to 0.01 s^{-1}. Firstly, the model is subjected to monotonic tensile and compressive loading at different values of asymmetry parameter, m. The results are plotted as stress-strain curves and depicted in Figure 22. As illustrated, increasing the value of m results in higher stress values. However, the effect of m is more pronounced under compression, and increasing m by 4% results in an increase of maximum stress by 12.5%. For a clearer overview, a one-cycle loading-unloading test is performed, and the corresponding stress-strain curve is shown in Figure 23. As observed, similarly, larger value of m yields higher stress levels, but plastic deformation exhibits almost no difference. Figures 24 and 25 demonstrate the model behavior under tensile-compression-unloading and compression-tensile-unloading at different m values, respectively. Figure 24 shows that m affects more the model responses under compression compared to the tensile zone, and the plastic deformation shifts to the right by increasing m. As illustrated in Figure 25, the effect of m is slightly more considerable in the tension zone than in the compression zone, however, its effect on the plastic deformation is not significant. In this section, the model has been investigated under tension-compression loading, and the effect of increasing asymmetry parameter on the stress-strain curves has been explored. In the next section, the model is implemented using a finite element model and a parametric study is carried out.

4.2. Asymmetric yield behavior under multi-axial loading using FE solver

The scope of this numerical analysis is to conduct a parametric study exploring the effect of the asymmetry parameter,m, on the mechanical response. The objective is to determine if this parameter influences the distribution of stresses, plasticity, and damage through asymmetrical behavior under biaxial loading. To this end, a notched structure with the loading and boundary conditions given in Figure 26 is considered. The structure is subjected to proportional biaxial displacement loading: compression in Y-axis and tension in X-axis. The displacement rate is set to 5 $mm\,s^{-1}$. The model parameters are those given in Table 2. The analysis is performed for three different values of the asymmetry parameter: $m = 1$, $m = 1.05$, $m = 1.2$. In all cases the total

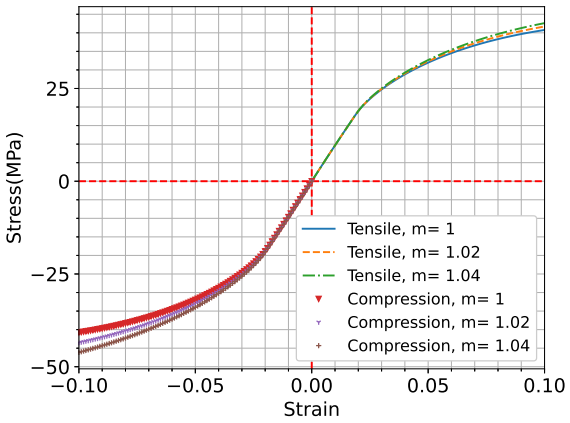

Figure 22: Stress-strain curves under monotonic tests using the 0D solver at different values of m. Under compressive loading, a 4% increase in m results in a 12.5% increase in the maximum stress.

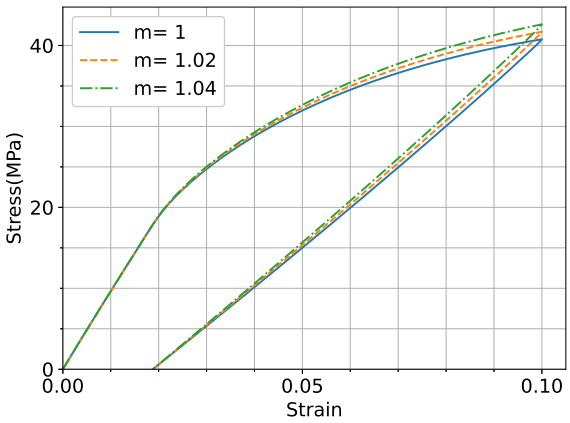

Figure 23: Stress-strain curves under loading-unloading tests using the 0D solver at different values of m.

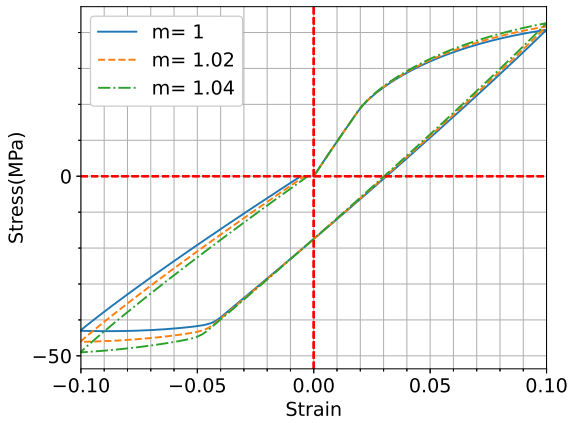

Figure 24: Stress-strain curves under tensile-compression tests using the 0D solver at different values of m. Under compressive loading, a 4% increase in m results in a 12.5% increase in the maximum stress.

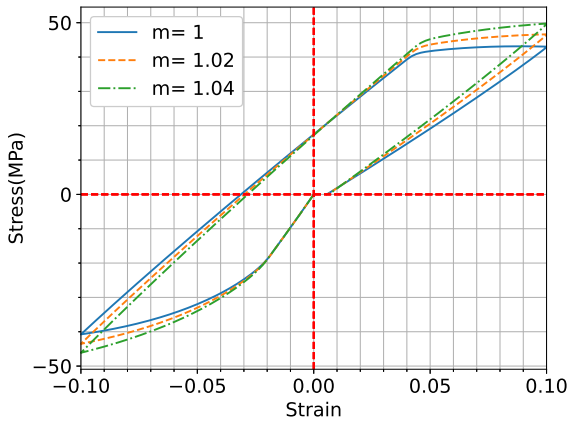

Figure 25: Stress-strain curves under compression-tension tests using the 0D solver at different values of m.

time is 0.58 s. The 3D maps of hardening state variable or plasticity and damage are plotted and depicted in Figure 27. As seen, the damage and plasticity level in the symmetric case when $m = 1$ is relatively higher than other cases. In other words, increasing m leads to a reduction in plasticity and consequently damage due to the increase in compressive yield strength.

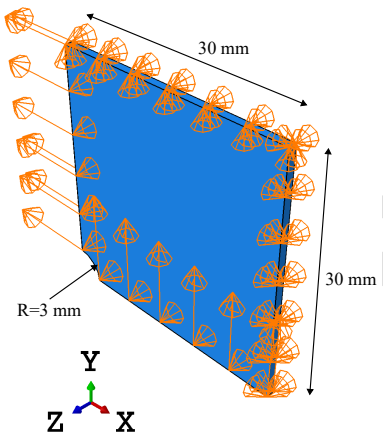

Figure 26: Dimensions, boundary conditions and biaxial loading conditions of the notched plate. The plate thickness is set to 1 mm.

5. Conclusions and future works

In this study, a thermodynamically consistent model, is proposed to capture the mechanical responses of polyamide 66. The model considers the following inelastic mechanisms that appear in the relevant material under moderate and high relative humidity conditions: viscoelasticity, pressure dependent viscoplasticity with tension-compression asymmetry, as well as ductile damage. The conclusions are summarized as follows:

- Mechanical tests on dogbone and diabolo-shaped samples revealed non-linear inelastic mechanisms as well as tension-compression asymmetry. The experimental findings were used to identify model parameters, and, for the first time, the asymmetry parameter, i.e. the ratio of compressive strength to tensile strength, was successfully identified through tension/torsion experimental data generated from diabolo specimens.

- Validation tests show overall good agreement between experimental and numerical responses.

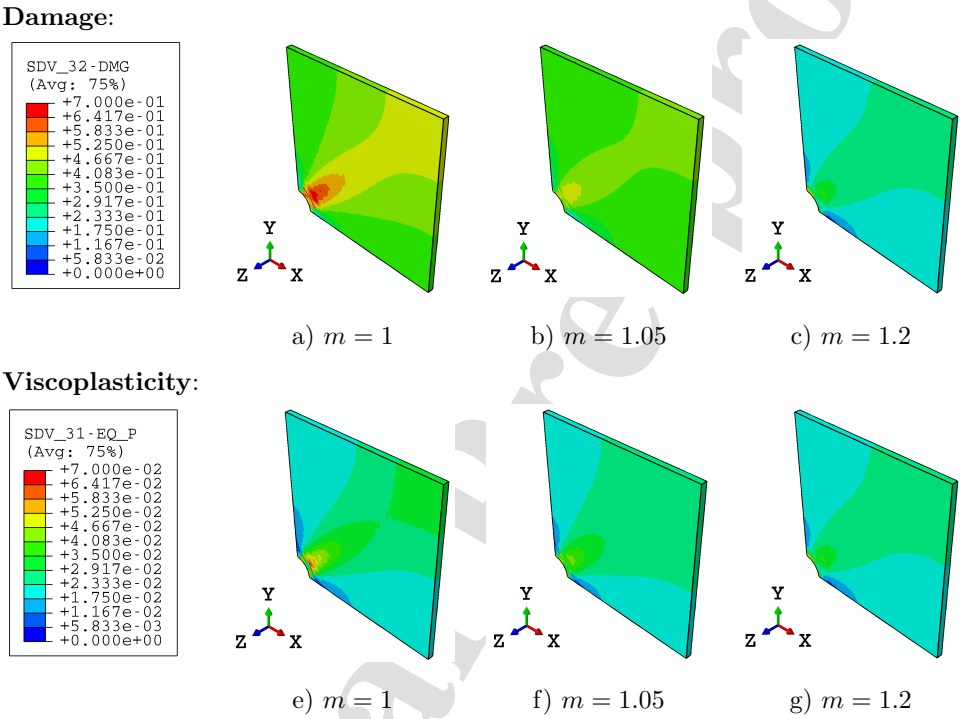

Figure 27: 3D maps of damage and viscoplasticity in the notched plate under biaxial (tension-compression) proportional loading at different m values. All profiles have been plotted at the same time (0.58 s). Considering tension/compression asymmetry ($m > 1$) leads to smoother distributions of damage and equivalent viscoplastic strain.

However, the discrepancies between numerical calculations and experimental data under certain loading conditions are relatively larger, which may be due to the geometric complexity of the diabolo specimens and also to the numerous mechanisms and mechanical tests involved in the parameter identification process.

- Parametric studies have shown how variation in m affects mechanical responses under compressive and tensile loading. Increasing m leads to asymmetry in stress-strain curves under tension-compression and compression-tension loading conditions. Furthermore, an increase in m results in less damage and plasticity, as observed in the 3D maps from the finite element computations.

This research can be extended to other aspects, such as hydrostatic pressure, composite materials and other environmental conditions, which are briefly discussed below:

- The model can be calibrated to account for the hydrostatic pressure effect, which requires additional mechanical tests on the water-filled samples.

- Considering the symmetrical yield behavior, VEVPD models have already been used in multi-scale models to estimate the overall mechanical responses of composites with short fiber thermoplastic composites (Barral et al., 2020; Chen et al., 2021; Praud et al., 2024; Chen et al., 2022) as well as for woven fabric composites (Tikarrouchine et al., 2018). The present framework can be integrated as a matrix in multi-scale mean-field or full-field homogenization models to analyze the overall mechanical responses of composites, taking into account tension-compression asymmetry and the hydrostatic pressure effect. In addition, the developed model can be associated with a data-driven multiscale modeling using artificial neural networks, such as the recent work by El Fallaki Idrissi et al. (2024).

- As polyamide is widely used in industry, it is subjected to a variety of environmental conditions. Thus, not only humidity affects their general behavior, but other chemicals, such as antifreeze (a mixture of water and ethylene glycol), also strongly influence their mechanical properties (Pires, 2000; Chekkour et al., 2023). The chemical effect can be accompanied with temperature change in some mechanical pieces, such as composites used in the cooling radiators Ledieu (2010). Therefore, in future research, the present model can be extended to consider chemo-thermal environmental conditions.

References

Abu Al-Rub RK, Tehrani AH, Darabi MK. Application of a large deformation nonlinear-viscoelastic viscoplastic viscodamage constitutive model to polymers and their composites. International Journal of Damage Mechanics 2015;24(2):198–244.

Barral M, Chatzigeorgiou G, Meraghni F, Léon R. Homogenization using modified mori-tanaka and tfa framework for elastoplastic-viscoelastic-viscoplastic composites: theory and numerical validation. International Journal of Plasticity 2020;127:102632. doi:10.1016/j.ijplas.2019.11.011.

Barrett R, O'donoghue P, Leen S. An improved unified viscoplastic constitutive model for strain-rate sensitivity in high temperature fatigue. International Journal of Fatigue 2013;48:192–204. doi:10.1016/j.ijfatigue.2012.11.001.

Benaarbia A, Chatzigeorgiou G, Kiefer B, Meraghni F. A fully coupled thermo-viscoelastic-viscoplastic-damage framework to study the cyclic variability of the taylor-quinney coefficient for semi-crystalline polymers. International Journal of Mechanical Sciences 2019;163:105128. doi:10.1016/j.ijmecsci.2019.105128.

Cailletaud G, Sai K. Study of plastic/viscoplastic models with various inelastic mechanisms. International Journal of Plasticity 1995;11(8):991–1005. doi:10.1016/s0749-6419(95)00040-2.

Chaboche J, Rousselier G. On the plastic and viscoplastic constitutive equations - Part I: Rules developed with internal variable concept. Journal of Pressure Vessel Technology 1983;doi:10.1115/1.3264257.

Chaboche JL. Thermodynamic formulation of constitutive equations and application to the viscoplasticity and viscoelasticity of metals and polymers. International Journal of Solids and Structures 1997;34(18):2239–54. doi:10.1016/s0020-7683(96)00162-x.

Chaboche JL. A review of some plasticity and viscoplasticity constitutive theories. International Journal of Plasticity 2008;24(10):1642–93. doi:10.1016/j.ijplas.2008.03.009.

Chekkour R, Benaarbia A, Chatzigeorgiou G, Meraghni F, Robert G. Effect of thermo-hygro glycol aging on the damage mechanisms of short glass-fiber reinforced polyamide 66. Composites Part A: Applied Science and Manufacturing 2023;165:107358. doi:10.1016/j.compositesa.2022.107358.

Chen Q, Chatzigeorgiou G, Meraghni F. Extended mean-field homogenization of viscoelastic-viscoplastic polymer composites undergoing hybrid progressive degradation induced by interface debonding and matrix ductile damage. International Journal of Solids and Structures 2021;210:1–17. doi:10.1016/j.ijsolstr.2020.11.017.

Chen Q, Chatzigeorgiou G, Robert G, Meraghni F. Viscoelastic-viscoplastic homogenization of short glass-fiber reinforced polyamide composites (pa66/gf) with progressive interphase and matrix damage: New developments and experimental validation. Mechanics of Materials 2022;164:104081. doi:10.1016/j.mechmat.2021.104081.

Chen Q, Chatzigeorgiou G, Robert G, Meraghni F. Combination of mean-field micromechanics and cycle jump technique for cyclic response of PA66/GF composites with viscoelastic-viscoplastic and damage mechanisms. Acta Mechanica 2023;234:1533–52. doi:10.1007/s00707-022-03448-4.

Chu C, Needleman A. Void nucleation effects in biaxially stretched sheets. Journal of Engineering Materials and Technology 1980;102(3):249–56. doi:10.1115/1.3224807.

Contesti E, Cailletaud G. Description of creep-plasticity interaction with non-unified constitutive equations: application to an austenitic stainless steel. Nuclear engineering and design 1989;116(3):265–80. doi:10.1016/0029-5493(89)90087-3.

Coulomb CA. essay on maximums and minimums of rules to some static problems relating to architecture. Academie Royale Des Sciences 1776;7:343–82.

Detrez F, Cantournet S, Seguela R. Plasticity/damage coupling in semi-crystalline polymers prior to yielding: Micromechanisms and damage law identification. Polymer 2011;52(9):1998–2008. doi:10.1016/j.polymer.2011.03.012.

Donato GHB, Bianchi M. Pressure dependent yield criteria applied for improving design practices and integrity assessments against yielding of engineering polymers. Journal of Materials Research and Technology 2012;1(1):2–7. doi:10.1016/s2238-7854(12)70002-9.

Drucker DC, Prager W. Soil mechanics and plastic analysis or limit design. Quarterly of applied mathematics 1952;10(2):157–65. doi:10.1090/qam/48291.

Dufour L, Bourel B, Lauro F, Haugou G, Leconte N. A viscoelastic-viscoplastic model with non associative plasticity for the modelling of bonded joints at high strain rates. International Journal of Adhesion and Adhesives 2016;70:304–14. doi:10.1016/j.ijadhadh.2016.07.015.

El Fallaki Idrissi M, Praud F, Meraghni F, Chinesta F, Chatzigeorgiou G. Multiscale Thermodynamics-Informed Neural Networks (MuTINN) towards fast and frugal inelastic computation of woven composite structures. Journal of the Mechanics and Physics of Solids 2024;186:105604. doi:10.1016/j.jmps.2024.105604.

Ghorbel E. A viscoplastic constitutive model for polymeric materials. International Journal of Plasticity 2008;24(11):2032–58. doi:10.1016/j.ijplas.2008.01.003.

Goutal C. Fatigue design of a short glass fibers reinforced thermoplastic (PA66GF50) with macroscopic singularities under uni- and multi-axial loadings. Ph.D. thesis; École nationale supérieure de mécanique et d'aérotechnique; 2020.

Gurson A. Continuum theory of ductile rupture by void nucleation and growth: Part i-yield criteria and flow rules for porous ductile media. Journal of Engineering Materials and Technology 1977;doi:10.1115/1.3443401.

Głowacka K, Kurek A, Smolnicki T, Łagoda T, Osiecki T, Kroll L. Change in elastic modulus during fatigue bending and torsion of a polymer reinforced with continuous glass fibers. Engineering Failure Analysis 2022;138:106341. doi:https://doi.org/10.1016/j.engfailanal.2022.106341.

Haddad M, Doghri I, Pierard O. Viscoelastic-viscoplastic polymer composites: Development and evaluation of two very dissimilar mean-field homogenization models. International Journal of Solids and Structures 2022;236:111354.

Halphen B, Nguyen Q. On the generalized standards materials (in french). Journal de Mécanique 1975;14:39–63.

Hasan O, Boyce MC. A constitutive model for the nonlinear viscoelastic viscoplastic behavior of glassy polymers. Polymer Engineering & Science 1995;35(4):331–44. doi:10.1002/pen.760350407.

Kachanov L. Time of the rupture process under creep conditions. Izvestiia Akademii Nauk SSSR, Otdelenie Teckhnicheskikh Nauk 1958;8:26–31.

Koplik J, Needleman A. Void growth and coalescence in porous plastic solids. International Journal of Solids and Structures 1988;24(8):835–53. doi:10.1016/0020-7683(88)90051-0.

Krairi A, Doghri I. A thermodynamically-based constitutive model for thermoplastic polymers coupling viscoelasticity, viscoplasticity and ductile damage. International Journal of Plasticity 2014;60:163–81. doi:10.1016/j.ijplas.2014.04.010.

Laiarinandrasana L, Morgeneyer TF, Proudhon H, Regrain C. Damage of Semicrystalline Polyamide 6 Assessed by 3D X-Ray Tomography: From Microstructural Evolution to Constitutive Modeling. Journal of Polymer Science: Part B: Polymer Physics 2010;48:1516–25. doi:10.1002/polb.22043.

Ledieu B. Vieillissement en milieu eau/glycol du polyamide 66 renforce fibres de verre courtes pour l'application boite a eau de radiateur de refroidissement moteur. Ph.D. thesis; Arts et Métiers ParisTech; 2010.

Lee Y, Ghosh J. The significance of J_3 to the prediction of shear bands. International Journal of Plasticity 1996;12(9):1179–97. doi:10.1016/s0749-6419(96)00047-2.

Lemaitre J. Coupled elasto-plasticity and damage constitutive equations. Computer methods in applied mechanics and engineering 1985;51(1-3):31–49. doi:10.1016/0045-7825(85)90026-x.

Magnenet V, Rahouadj R, Ganghoffer JF, Cunat C. Continuous symmetry analysis of a dissipative constitutive law: application to the time-temperature superposition. European Journal of Mechanics-A/Solids 2009;28(4):744–51. doi:10.1016/j.euromechsol.2009.02.002.

Manaia JP, Pires FA, De Jesus AM, Wu S. Mechanical response of three semi crystalline polymers under different stress states: Experimental investigation and modelling. Polymer Testing 2020;81:106156. doi:10.1016/j.polymertesting.2019.106156.

Miled B, Doghri I, Delannay L. Coupled viscoelastic–viscoplastic modeling of homogeneous and isotropic polymers: Numerical algorithm and analytical solutions. Computer Methods in Applied Mechanics and Engineering 2011;200(47-48):3381–94. doi:10.1016/j.cma.2011.08.015.

Mises Rv. Mechanik der festen Körper im plastisch-deformablen Zustand. Nachrichten von der Gesellschaft der Wissenschaften zu Göttingen, Mathematisch-Physikalische Klasse 1913;1913:582–92.

Morin D, Haugou G, Bennani B, Lauro F. Experimental characterization of a toughened epoxy adhesive under a large range of strain rates. Journal of Adhesion Science and Technology 2011;25(13):1581–602. doi:10.1163/016942410x524417.

Nachtane M, Meraghni F, Chatzigeorgiou G, Harper L, Pelascini F. Multiscale viscoplastic modeling of recycled glass fiber-reinforced thermoplastic composites: Experimental and numerical investigations. Composites Part B: Engineering 2022;242:110087. doi:10.1016/j.compositesb.2022.110087.

Nelder JA, Mead R. A simplex method for function minimization. The computer journal 1965;7(4):308–13. doi:10.1093/comjnl/7.4.308.

Obeid H. Durabilité de composites à matrice thermoplastique sous chargement hygro-mécanique: étude multi-physique et multi-échelle des relations microstructure-propriétés-états mécaniques. Ph.D. thesis; Nantes; 2016.

Olufsen S, Clausen A, Hopperstad O. Influence of stress triaxiality and strain rate on stress-strain behaviour and dilation of mineral-filled pvc. Polymer Testing 2019;75:350–7. doi:10.1016/j.polymertesting.2019.02.018.

Ottosen NS, Ristinmaa M. The mechanics of constitutive modeling. Elsevier, 2005.

Pae K, Bhateja S. The effects of hydrostatic pressure on the mechanical behavior of polymers. Journal of Macromolecular Science, Part C 1975;13(1):1–75. doi:10.1080/15321797508068145.

Pipkin A, Rogers T. A non-linear integral representation for viscoelastic behaviour. Journal of the Mechanics and Physics of Solids 1968;16(1):59–72. doi:10.1016/0022-5096(68)90016-1.

Pires I. Vieillissement dans l'antigel de matériaux composites polyamide-6, 6 renforcé par des fibres de verre courtes. Ph.D. thesis; Montpellier 2; 2000.

Pivdiablyk I, Rozycki P, Jacquemin F, Gornet L, Auger S. Experimental analysis of mechanical performance of glass fibre reinforced polyamide 6 under varying environmental conditions. Composite Structures 2020;245:112338. doi:10.1016/j.compstruct.2020.112338.

Praud F, Chatzigeorgiou G, Bikard J, Meraghni F. Phenomenological multi-mechanisms constitutive modelling for thermoplastic polymers, implicit implementation and experimental validation. Mechanics of Materials 2017;114:9–29. doi:10.1016/j.mechmat.2017.07.001.

Praud F, Schneider K, Chatzigeorgiou G, Meraghni F. Microstructure generation and full-field multi-scale analyses for short fiber reinforced thermoplastics: Application to PA66GF composites. Composite Structures 2024;341:118175. doi:10.1016/j.compstruct.2024.118175.

Rabotnov Y. Creep rupture; Springer Berlin Heidelberg. p. 342–9. doi:10.1007/978-3-642-85640-2_26.

Raghava R, Caddell R, Yeh G. The macroscopic yield behaviour of polymers. Journal of Materials Science 1973;8(2):225–32. doi:10.1007/bf00550671.

Raghavan P, Ghosh S. A continuum damage mechanics model for unidirectional composites undergoing interfacial debonding. Mechanics of materials 2005;37(9):955–79. doi:10.1016/j.mechmat.2004.10.003.

Reuvers MC, Kulkarni S, Boes B, Felder S, Wutzler A, Johlitz M, Lion A, Brepols T, Reese S. A thermo-mechanically coupled constitutive model for semi-crystalline polymers at finite strains: Mechanical and thermal characterization of polyamide 6 blends. Continuum Mechanics and Thermodynamics 2024;36:657–98. doi:10.1007/s00161-024-01288-2.

Rivlin R. Integral representations of constitutive equations; Springer New York; volume 22. p. 1615–22. doi:10.1007/978-1-4612-2416-7_101.

Satouri S, Chatzigeorgiou G, Benaarbia A, Meraghni F. A gradient enhanced constitutive framework for the investigation of ductile damage localization within semicrystalline polymers. International Journal of Damage Mechanics 2022;31(10):1639–75. doi:10.1177/10567895221115459.

Satouri S, Chatzigeorgiou G, Benaarbia A, Meraghni F. Gradient enhanced multi-scale modeling framework for glass fiber reinforced polyamides. International Journal of Solids and Structures 2023a;267:112143. doi:10.1016/j.ijsolstr.2023.112143.

Satouri S, Chekkour R, Chatzigeorgiou G, Meraghni F, Robert G. Numerical-experimental approach to identify the effect of relative humidity on the material parameters of a rate-dependent damage

model for polyamide 66. Mechanics of Materials 2023b;184:104735. doi:10.1016/j.mechmat.2023.104735.

Schapery RA. Nonlinear viscoelastic and viscoplastic constitutive equations based on thermodynamics. Mechanics of Time-Dependent Materials 1997;1(2):209–40.

Simo JC, Hughes TJ. Computational inelasticity. volume 7. Springer Science & Business Media, 2006.

Singer S, Nelder J. Nelder-Mead algorithm. Scholarpedia 2009;4(7):2928. doi:10.4249/scholarpedia.2928; revision #91557.

Tikarrouchine E, Chatzigeorgiou G, Praud F, Piotrowski B, Chemisky Y, Meraghni F. Three-dimensional FE^2 method for the simulation of non-linear, rate-dependent response of composite structures. Composite Structures 2018;193:165–79. doi:10.1016/j.compstruct.2018.03.072.

Tresca H. Memoire sur l'écoulement des solides à de forte pressions. Acad Sci Paris 1864;2(1):59.

Tvergaard V, Needleman A. Effects of nonlocal damage in porous plastic solids. International Journal of Solids and Structures 1995;32(8-9):1063–77. doi:10.1016/0020-7683(94)00185-y.

Uchida M, Yoshida T, Okada E, Touji M, Kaneko Y. Mechanical modeling of polyamide 6 obtained from different thermal histories. Polymer 2024;:126770doi:10.1016/j.polymer.2024.126770.

Velay V, Bernhart G, Penazzi L. Cyclic behavior modeling of a tempered martensitic hot work tool steel. International Journal of Plasticity 2006;22(3):459–96. doi:10.1016/j.ijplas.2005.03.007.

Wang J, Peng L, Deng Y, Lai X, Fu M, Ni J. A finite strain thermodynamically-based constitutive modeling and analysis of viscoelastic-viscoplastic deformation behavior of glassy polymers. International Journal of Plasticity 2019;122:135–63. doi:10.1016/j.ijplas.2019.06.013.

Ward I. Review: The yield behaviour of polymers. Journal of Materials Science 1971;6(11):1397–417. doi:10.1007/bf00549685.

Zine A, Benseddiq N, Naït Abdelaziz M. Rubber fatigue life under multiaxial loading: Numerical and experimental investigations. International Journal of Fatigue 2011;33(10):1360–8. doi:https://doi.org/10.1016/j.ijfatigue.2011.05.005.

Highlights:

1- Nonlocal multi-scale framework for composite materials accounting for viscoelasticity, viscoplasticity, and ductile damage.
2- Multi-scale analysis depending on the relation between RVE size and the nonlocal phenomena characteristic length.
3- Investigation of the localization phenomena at the macroscale taking into account the microstructure.
4- Combining for the first time mean-field homogenization technique and nonlocal ductile damage.
5- Validation of the framework against full scale analysis and parametric investigation of the nonlocal composite response.

AUTHORSHIP STATEMENT Manuscript title:

Viscoelastic-viscoplastic model with ductile damage accounting for tension-compression asymmetry and hydrostatic pressure effect for polyamide 66

Soheil Satouri: Writing - Original Draft, Formal Analysis, Investigation, Validation

George Chatzigeorgiou: Formal Analysis, Writing - Review & Editing, Conceptualization, Investigation

Fodil Meraghni: Conceptualization, Methodology, Formal Analysis, Writing - Review & Editing, Project administration

Gilles Robert: Investigation, Resources, Data curation